A NEW LARGE-SCALE MAP OF THE LUNAR CRUSTAL MAGNETIC FIELD AND ITS INTERPRETATION. L. L. Hood[1], C. B. Torres[1], J. S. Oliveira[2], M. A. Wieczorek[3], and S. T. Stewart[4], [1]Lunar and Planetary Laboratory, University of Arizona, Tucson, Arizona, 85721, USA, lon@lpl.arizona.edu, [2]Space Magnetism Area, Payloads & Space Sciences Department, National Institute for Aerospace Technology, Torrejón de Ardoz, Spain, [3]Université Côte d'Azur, Observatoire de la Côte d'Azur, CNRS, Laboratoire Lagrange, Nice, France, [4]Dept. of Earth and Planetary Sciences, University of California, Davis.

Introduction: The origin of lunar magnetic anomaly sources remains controversial with some groups suggesting magnetized igneous bodies such as dike intrusions (e.g., [1], [2], [3]) and other groups suggesting magnetized impact basin or crater melt sheets and ejecta deposits (e.g., [4], [5], [6]).

Several valuable large-scale maps of the crustal magnetic field have already been produced using data from the Lunar Prospector (LP) and Kaguya (KG) polar orbiting missions (e.g., [7], [8], [9]). However, an alternate approach is to construct maps of improved accuracy over individual regions by selecting only the best measurements (lowest altitude with least amount of external field contamination) over those specific regions. Once the best measurements are identified, an equivalent source dipole (ESD) technique (e.g., [10], [11]) can be applied to normalize the measurements to a constant altitude. Individual regional maps can then be joined together to produce a large-scale map.

A map of the crustal field has recently been constructed using the latter methodology at 30 km altitude covering latitudes from 65°S to 65°N [12]. A digital version is available: https://doi.org/10.17189/1520494. In many respects, the map agrees well with the previous global map of [8]. However, one important difference is that the new map more accurately depicts the distribution of weaker anomalies. These weaker anomalies are important for understanding the likely origin of both strong and weak anomalies.

Relationship of Anomalies to Imbrium: Figure 1 shows a map of the central near side at 30 km altitude produced using the new methodology. For simplicity, only KG data were employed at all latitudes and longitudes. The contour interval is 0.5 nT starting at 1 nT. Noticeable in the figure is a tendency for anomalies to be aligned radial to the Imbrium basin (dashed lines). It has previously been noted that the Rima Sirsalis and Reiner Gamma anomalies tend to be oriented radial to the center of Imbrium (e.g., [13]). As seen in the figure, at this resolution (~ 2.5° latitude by ~ 5° longitude), the Reiner Gamma anomalies are extended in such a direction. Also, a further extension of this line passes through the Hartwig anomaly. As indicated by the other dashed lines, two other groups of weaker anomalies appear to also be aligned radial to Imbrium. One group is centered at ~18°S, 3°E (the "Airy group") and the other is centered at ~ 8°S, 45°E (the "Eastern group"). Note that the two Crisium anomalies, one of which is somewhat elongated, are not considered here because they most probably have sources originating at the time of the Crisium impact (e.g., [14]).

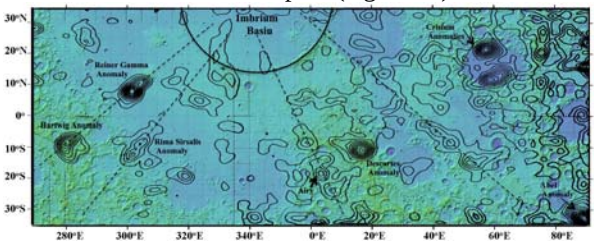

Figure 1

There is also evidence that relatively strong isolated anomalies on the southern near side tend to be aligned with anomaly groups that are elongated radial to Imbrium. Figure 2 is a plot similar to that of Figure 1 but with its southern boundary at 65°S. The contour interval is 0.5 nT starting at 0.5 nT. Because of the cylindrical projection, lines extending radially outward from Imbrium are not straight except at low latitudes. At this scale, it is therefore necessary to calculate great circle paths to investigate whether isolated anomalies lie along such lines. This is done by first selecting "end points" in a given elongated group and then evaluate whether the resulting great circle path passes near the center of Imbrium or near other mapped anomalies.

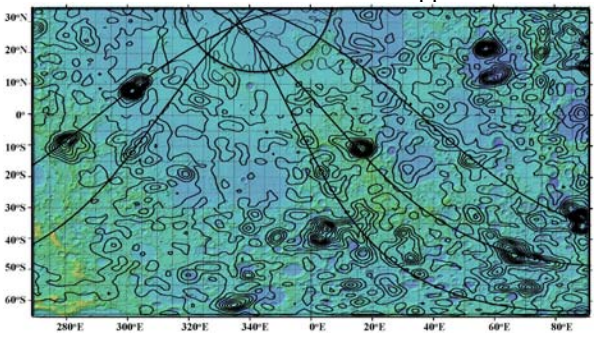

Figure 2

As seen Figure 2, the great circle path determined for the Eastern anomaly group curves northward to pass through the Abel anomaly located at 33°S, 88°E (~ 5.2 basin radii from the center of Imbrium). As seen in the southeastern corner of the map, a relatively strong but unnamed anomaly group is present near 45°S, 66°E (~ 4.9 basin radii from the center of Imbrium). Choosing end points at this location and at the Descartes anomaly (11°S, 16.5°E), the corresponding

great circle path also passes near the center of Imbrium. Finally, the unnamed anomaly group is extended radially outward from Imbrium along the great circle path. It therefore represents a fifth elongated anomaly group on the southern near side that is aligned radial to Imbrium. Monte Carlo simulations confirm that these alignments with Imbrium have only a small probability of occurring by chance [12].

Great circle paths that pass near the center of Imbrium must necessarily pass near the Imbrium antipode. Figure 3 confirms that this is the case by plotting them on the full large-scale map. The five paths passing through the elongated anomalies oriented radial to Imbrium on the southern near side intersect in the Imbrium antipode zone where the strongest group of anomalies is found.

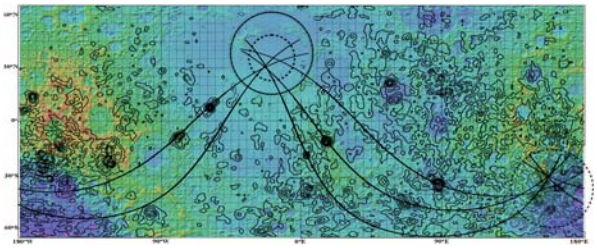

Figure 3

Discussion: On the basis of these results, it is suggested that the Imbrium impact played a role in the origin of many of the strongest magnetic anomalies on the Moon.

Several hypotheses for the origin of anomalies aligned radial to an impact basin are possible. First, the Imbrium impact may have produced radial fractures that led to later magmatic intrusions that are the anomaly sources. For example, the Rima Sirsalis anomaly lies near an extensional graben that probably resulted from lithospheric stresses related to the formation of Imbrium. However, while Rima Sirsalis is located only a few basin radii from the center of Imbrium, many of the radially aligned anomalies identified here (e.g., Abel) are located at distances of thousands of km from the basin. A tectonic-related origin for these anomalies involving magmatic intrusions is less plausible.

Second, ejecta from the Imbrium impact may have been enriched in iron from the impactor and was deposited in groups that tended to align radial to the basin. Some support for this hypothesis comes from numerical simulations of lunar basin formation via the impact of iron-rich planetesimals reported by Wieczorek et al. [5]. These simulations, which used a CTH shock physics code in three dimensions with self-gravity, were for the special case of the SPA basin-forming impact. However, simulations for smaller basins such as Imbrium should give qualitatively similar results although the details may be different. These simulations showed that for oblique impacts (more than 50^{o} from the vertical), most of the iron-enriched melt was deposited inhomogeneously downrange of the basin interior. Several simulations (see the supporting material) showed alignments of iron-enriched ejecta deposits radial to the basin center. The inhomogeneous mixture of impactor iron into some ejecta deposits but not others demonstrated in these simulations provides an explanation for why some great circle paths and not others show anomalies aligned radial to Imbrium.

Accepting the iron-enriched ejecta explanation for the radially aligned nearside anomalies, it follows that the cluster of strong anomalies in the Imbrium antipode zone is probably a consequence of convergence of such ejecta at the antipode. The antipodal zones of several young lunar basins contain unusual hilly and lineated terrain that correlates with the occurrence of magnetic anomalies (e.g., the walls of the Ingenii basin at the Imbrium antipode) [15] [16]. The origin of the unusual terrain continues to be debated but impacts of converging ejecta and secondaries in these regions may have played an important role [17] [18].

Acknowledgments: Lunar Prospector calibrated magnetometer data are available from the PPI node of the NASA PDS (https://pds-ppi.igpp.ucla.edu). Kaguya (SELENE) vector magnetometer data are available from the Japan Aerospace Exploration Agency at http://darts.isas.jaxa.jp/planet/pdap/selene.

References: [1] Purucker M. E. et al. (2012) *JGR, 117*, https://doi.org/10.1029/2011JE003922. [2] Tsunakawa H. et al. (2014) *Icarus, 228*, 35-53. [3] Hemingway D. J. & Tikoo S. M. (2018) *JGR Planets, 123*, 2223-2241. [4] Hood L. L. et al. (2001) *JGR 106*, 27825-27839. [5] Wieczorek M. A. et al. (2012) *Science, 335*, 1212-1215. [6] Garrick-Bethell I. & Kelley M. R. (2019) *GRL, 46*, 5065-5074. [7] Purucker M. E. & Nicholas J. B. (2010) *JGR, 115*, https://doi.org/ 10.1029 /2010JE003650. [8] Tsunakawa H. et al. (2015) *JGR Planets, 120*, 1160-1185. [9] Ravat D. et al. (2020) *JGR Planets, 125*, https://doi.org/10.1029/ 2019JE006187. [10] Mayhew M. A. (1979), *Geophys. J., 45*, 119-128. [11] von Frese R. R. B. et al. (1981) *Earth Planet. Sci. Lett., 53*, 69-83. [12] Hood L. L. et al. (2021a) *JGR Planets, 126*, https://doi.org/10.1029/ 2020JE006667. [13] Halekas J. S. et al. (2001) *JGR, 106*, 27841-27852. [14] Hood L. L. et al. (2021b) *JGR Planets, 126*, https://doi.org/10.1029/2020JE006668. [15] Richmond N. C. et al. (2005) *JGR*, https://doi.org/ 10.1029/ 2005JE002405. [16] Hood L. L. et al. (2013) *JGR Planets, 118*, https://doi.org/10.1002/jgre.20078. [17] Moore H. J. et al. (1974) *Proc. 5th LPSC*, 71-100. [18] Hood L. L. & Artemieva N. (2008) *Icarus, 197*, 485-502.